3D-printed Strontium-Titanium Scaffolds Incorporated with Highly Bioactive Serum Exosomes Promotes Critical Bone Defect Repair by Enhancing Osteogenesis and Angiogenesis

Hao Liu
Peking University Hospital of Stomatology
Ranli Gu
Peking University School of Stomatology Department of Prosthodontics
Wei Li
Peking University Hospital of Stomatology
Lijun Zeng
Peking University School of Stomatology Department of Prosthodontics
Yuan Zhu
Peking University School of Stomatology Department of Prosthodontics
Siyi Wang
Peking University School of Stomatology Department of Prosthodontics
Xuenan Liu
Peking University School of Stomatology Department of Prosthodontics
Boon Chin Heng
Peking University School of Stomatology Department of Prosthodontics
Yunsong Liu (liuyunsong@hsc.pku.edu.cn)
Peking University Hospital of Stomatology https://orcid.org/0000-0003-3374-2097
Yongsheng Zhou
Peking University School of Stomatology Department of Prosthodontics

Research Article

Keywords: scaffolds, strontium, exosomes, osteogenesis, angiogenesis

Posted Date: October 27th, 2022

DOI: https://doi.org/10.21203/rs.3.rs-2141014/v1

Abstract

Background

Large bone defect healing faces significant challenges because of inadequate bone regeneration and revascularization. Serum exosomes (sEXO) during bone defect repair are rich in osteogenic factors. Titanium (Ti) scaffolds and low dose strontium (Sr) can promote bone regeneration. Here, a “cell-free scaffold engineering” strategy that incorporates strontium and highly bioactive sEXO within a 3D-printed Ti scaffold is developed.

Methods

Sr-Ti-sEXO composite was prepared by ion implantation and ultra-high-speed centrifugation. Alkaline phosphatase (ALP), Alizarin red (ARS), immunofluorescence (IF) staining, and polymerase chain reaction (PCR) were used to detect the osteogenic effect of Sr-Ti-sExo on bone marrow mesenchymal stem cells (BMSCs). Tartrate-resistant acid phosphatase (TRAP) staining, and PCR were used to detect the osteoclast effect of Sr-Ti-sEXO on RAW264.7. The vascularization effect of Sr-Ti-sEXO on human umbilical vein endothelial cells (HUVECs) was investigated by scratch and migration experiments. Micro-CT and histological staining were used to study the osteogenic and vasculogenic effects of Sr-Ti-sEXO implanted in rabbit large radius defect at 6 and 12 weeks *in vivo*. RNA-seq was used to explore the potential mechanism.

Results

Sr-Ti-sEXO composite promoted early osteogenesis and inhibited osteoclast formation through the combined release of Sr ions and sEXO, and sustained release of Sr ions enhanced bone conduction, bone induction and inhibited fibroblasts. sEXO can promote the vascular reconstruction of CBD in fracture stage, which has the dual effect of promoting bone and promoting angiogenesis in critical bone defect repair. These effects are regulated by multiple miRNAs that shuttle in sEXO.

Conclusions

Sr-Ti-sEXO has favourable sustained release performance, osteogenic and vasogenic effects, which is a biocompatible and clinically feasible critical bone defect repair strategy. This study also broadens the biomedical potential of exosomes with specific functions such as sEXO in fracture stage. Based on the relative abundance of sEXO, a sEXO library for clinical treatment can be established.

1. Introduction

Critical bone defects (CBD) resulting from tumors, trauma, infections, or congenital disorders still present a formidable clinical challenge, with particularly high risks of complications such as nonunion, malunion, and deep infection [1]. Deficient bone regeneration and revascularization of bone defect regions are major challenges in orthopedic surgery, especially for large bone defects that are incapable of spontaneous healing. Clinically, large bone defects can be treated by bone grafts from an autologous or xenogenic source, but there are many limitations such as shortage of donor sources, disease transmission, and immune rejection [2].

Recently, 3D-printed titanium (Ti) scaffolds have been increasingly utilized for customized treatment of large bone defects [3]. However, there are still many challenges to be overcome, before satisfactory osseointegration can be achieved, mainly due to the inherent bio-inertness and lack of osteoinductivity of titanium [4]. Alternatively, strontium (Sr) ions at physiological concentration can act as a bioactive factor in promoting bone formation and inhibiting bone resorption [5]. Controlled-released of Sr ions from the superficial layer of the scaffold can be a clinically feasible therapeutic strategy for repairing large bone defects.

Achieving vascular and osteoid reconstruction at the initial stage are a crucial step for bone defect healing. In recent years, exosomes have been increasingly applied in cell-free bone regeneration strategies owing to their good biocompatibility, low immunogenicity and negligible cytotoxicity [6]. To achieve good osteoinductivity, exosomes were obtained from osteogenic differentiation of mesenchymal stem cells (MSCs) that was induced by chemical compounds in *vitro*, prior to being utilized for treatment of bone defects in *vivo* [7]. However, osteogenic exosomes induced by chemical compounds rather than the natural osteogenic microenvironment, may have limited clinical translation potential due to safety issues and other possible side effects.

Intriguingly, specifically functionalized body fluid has recently exhibited promising therapeutic potential for some intractable diseases. For example, Iram *et. al.* demonstrated that infusing young cerebrospinal fluid (CSF) directly into aged brains improved memory function because fibroblast growth factor 17 (Fgf17) from young CSF restored oligodendrocyte function within the ageing brain of mice [8]. Moreover, another landmark research also showed that exposure to young blood through heterochronic parabiosis induced stem cell revitalization and systemic rejuvenation of aged mice tissues, which can be attributed to blood-borne factors [9]. An interesting study demonstrated that, serum exosomes (sEXO), an abundant type of body fluid exosomes, can promote angiogenesis and protect against myocardial ischaemia due to the presence of a large number of angiogenic factors [10, 11]. However, it is inadequate for effectively promoting bone formation. Several clinical and pre-clinical studies have validated that serum produced during the fracture healing process contains abundant amounts of osteogenic factors including collagen X, 25(OH)D, bone morphogenetic protein-2 (BMP-2), as well as angiogenic factors including HIF-1α [12–15]. Therefore, sEXO derived from fracture repair stage (BF EXO) may contain more RNAs and protein-based growth factors that can enhance angiogenesis and osteogenesis.

Poloxamers are thermo-responsive polymers, characterized by good solubility, negligible toxicity, excellent controlled release capacity, and good compatibility with various biomolecules and chemical excipients. Therefore, poloxamers 407 (P407) and 188 (P188) are widely used for the administration of drug and biomolecules through various routes [16]. Hence, a poloxamer-based hydrogel may be used to facilitate the controlled release of BF EXO *in situ*, to promote osteogenesis and angiogenesis.

Here, we utilize a “scaffold engineering” strategy that incorporates both BF EXO and Sr within a 3D-printed titanium (Ti) scaffold (Sc), for CBD repair (Scheme 1). The porous Ti Sc were printed by mimicking the radial CBD region and Sr was injected into the superficial layer of the scaffolds by ion implantation. Moreover, the dual effects of SrTi Sc on enhancing osteogenesis and inhibiting bone resorption were evaluated. Additionally, the pro-osteogenic and pro-angiogenic capacities of BF EXO extracted from the serum of a femoral fracture rabbit model during the fracture healing stage were evaluated, followed by RNA sequencing and bioinformatics analysis. Subsequently, SrTi Sc + BF EXO composites were implanted into the radial CBDs of rabbits to evaluate their efficacy in promoting osteogenesis and vascularization in *vivo*. Our study thus broadens the mode of delivery and biomedical potential of specifically functionalized exosomes, as well as provides a comprehensive and clinically feasible strategy for the treatment of large bone defects.

2. Results

2.1. Fabrication and Characterizations of SrTi Sc

As shown in Scheme 1, the 3D-printed Ti Sc was successfully fabricated according to the shape of the radius midshaft, and Sr was subsequently implanted into the superficial layer of the scaffolds. The microstructures of Ti Sc and SrTi Sc were similar, as observed with a stereoscope, microCT, mercury porosimeter, N_2-BET device, and scanning electron microscopy (SEM) (**Figure S1, Tables S1 and S2, Supporting Information**). However, there were more numerous minuscule sediments attached to Ti particles in SrTi Sc compared to Ti Sc, as observed under SEM (Fig. 1A). Furthermore, 4.7% Sr (Wt %) exists on the surface of SrTi Sc, as detected by energy dispersive spectroscopy (EDS) (**Figure S2, Supporting Information**). Additionally, the data of Sr controlled release from SrTi Sc, as detected by inductive coupled plasma emission spectrometer (ICP) in *vitro*, showed that Sr was quickly dissolved in PBS within 10 days, but was subsequently released slowly between 10–28 days, and then separated out in trace amounts from 28 days to 84 days (Fig. 1B). In addition, the biomechanical properties of Ti Sc and SrTi Sc were significantly better than those of the rabbit radius. Except for Young’s modulus in the compression test, there were no significant differences in biomechanical parameters between Ti Sc and SrTi Sc (**Table S3, Supporting Information**).

2.2. Ability on Promoting Osteogenesis and Inhibiting Osteoclastogenesis of SrTi Sc *in Vitro*

To test whether the SrTi Sc had better bidirectional effects than Ti Sc, assays on osteogenesis and inhibition of osteoclastogenesis were performed. Compared with Ti Sc, the leach liquor of SrTi Sc significantly enhanced the osteogenic differentiation of bone marrow-derived mesenchymal stem cells (BMSCs), as indicated by alkaline phosphatase (ALP)/ alizarin red (ARS) (two key osteogenic markers) staining and quantification (Fig. 1C **and D; Figure S3A and B, Supporting Information**). Moreover, the SrTi Sc group also displayed significantly increased gene expression of osteogenesis markers (*SPARC*, *ALPL, RUNX2*, and *SPP1*), as compared to the Ti Sc group (Fig. 1E; **Figure S3C, Supporting Information**).

Besides, the results of tartrate resistant acid phosphate (TRAP) staining/quantification and immunostaining of osteoclast-like cells (OLCs, RANKL-induced RAW 264.7 cells) showed that the leach liquor of SrTi Sc significantly lessened numbers of OLCs, as compared to that of Ti Sc (Fig. 1F **and G; Figure S4A and B, Supporting Information**). Consistent with the cytological experiment, the gene expression levels of bone resorption markers (*Rank*, *Rankl*, and *Trap*) showed a similar tendency (Fig. 1H; **Figure S4C, Supporting Information**).

Additionally, based on the CCK-8 assay, the leach liquor of SrTi Sc effected greater enhancement of the cell proliferation rate of BMSCs, and slowed down proliferation of OLCs more than the Ti Sc group, after 3 days of co-culture (Fig. 1I; **Figure S5, Supporting Information**). However, the L929 cell viability of the SrTi Sc group was significantly decreased by 5.54%, as compared with that of the Ti Sc group at 72 h (**Figure S6, Supporting Information**).

2.3. Characterizations of BF EXO

Scheme 1 also showed that BF EXO was extracted from the serum of rabbits during the period of femoral fracture healing. Meanwhile, CTRL EXO was obtained likewise from healthy rabbits in a similar manner. In accordance with the characteristics of CTRL EXO, BF EXO also exhibited a spherical microvesicle structure, as observed under transmission electron microscope (TEM) (Fig. 2A). Western blot analysis revealed that the typical exosome surface markers TSG101, CD81, and CD9 were expressed on both CTRL and BF EXO (**Figure S7A, Supporting Information**). Moreover, the size and concentration of both CTRL and BF EXO was approximately 55–110 nm and 1.09–1.15 particles / mL serum, respectively, as detected by Nanosight NS300 (**Figure S7B, Supporting Information**). Moreover, both CTRL and BF EXO could be taken up by BMSCs (**Figure S8, Supporting Information**). Unlike Sr controlled release, BF EXO was gradually and continuously released from a poloxamers-based hydrogel that finally lasted for 96 h (Fig. 2B; **Table S4, Supporting Information**).

2.4. Ability on Promoting Osteogenesis and Inhibiting Osteoclastogenesis of BF EXO *in Vitro*

Moreover, the osteogenesis of BF EXO was significantly enhanced, as compared with that of CTRL EXO, as evaluated by ALP/ARS staining and quantification, and expression of osteogenesis-related genes (Fig. 2C-E; **Figure S9, Supporting Information**). In contrast, the representative images of TRAP/ immunofluorescence staining and quantification showed that the BF EXO group had lesser number of

osteoclasts than that of the CTRL EXO group, based on the standard of TRAP-positive cells with more than three nuclei being considered as osteoclasts (Fig. 2F **and G; Figure S10A-B, Supporting Information**). Moreover, the expression of osteoclastogenesis-related genes including *Rank*, *Rankl*, and *Trap* in the BF EXO group were significantly more downregulated, as compared to those of the CTRL EXO group (Fig. 2H; **Figure S10C, Supporting Information**).

Intriguingly, the BF EXO significantly enhanced the proliferation of BMSCs and inhibited the formation of OLCs, as compared with CTRL EXO, as shown by the CCK-8 assay (Fig. 2I; **Figure S11, Supporting Information**).

2.5. Ability on Angiogenesis of BF EXO *in Vitro* and *in Vivo*

Furthermore, the effects of BF EXO on angiogenesis were evaluated by *in vitro* and *in vivo* assays using human umbilical vein endothelial cells (HUVECs). As depicted in Fig. 3A **and B**, the rate of scratch wound closure in the BF EXO group was higher than that of the CTRL EXO group, as detected by scratch test (**Figure S12, Supporting Information**). Furthermore, the numbers of migrating cells in the BF EXO group were more than those in the CTRL EXO group, as shown by the transwell assay (Fig. 3A **and C; Figure S13, Supporting Information**). Additionally, *in vitro* tube formation of HUVECs on the matrigel layer was employed to evaluate the revascularization capacity. Compared with the CTRL EXO group, the total segment length, total mesh area, and total branching length composed of HUVECs were significantly higher in the BF EXO group (Fig. 3A **and D; Figure S14, Supporting Information**). Moreover, *in vivo* angiogenesis assays through subcutaneous injection of matrigel plugs containing BF EXO/CTRL EXO or addition of BF EXO/CTRL EXO into chicken chorioallantois membrane (CAM) showed that BF EXO had a better angiogenic induction capacity than CTRL EXO (Fig. 3E **and F; Figure S15 and S16, Supporting Information**). Meanwhile, the qPCR results demonstrated that BF EXO significantly enhanced the relative expression of angiogenic-related genes including *VEGFA*, *TGFβ*, *MMP2*, and *VEGFR2*, as compared with CTRL EXO (Fig. 3G; **Figure S17, Supporting Information**). Additionally, in the CCK-8 assays, BF EXO treatment increased proliferation of HUVECs significantly more than CTRL EXO (Fig. 3H; **Figure S18, Supporting Information**).

2.6. Mechanism for Osteogenesis and Vascularization of BF EXO

To explore the potential mechanisms by which BF EXO promote both osteogenesis and vascularization, differential expression of exosome-shuttled miRNAs between BF EXO and CTRL EXO was analyzed by next generation sequencing (NGS). The volcanic map of miRNA expression showed that 59 miRNAs were upregulated, whereas 85 miRNAs were downregulated in the BF EXO group, as compared with the CTRL EXO group (Fig. 4A). As depicted in Fig. 4B, osteogenic miRNAs, such as Ocu-miR-122-5p, Ocu-miR-486-5p, Ocu-miR-93-5p, Ocu-miR-25-3p, Ocu-miR-10a-3p, Ocu-miR-142-5p, and Ocu-miR-92a-3p were upregulated in the BF EXO group, as compared with the CTRL EXO group. By contrast, there were significantly downregulated miRNAs inhibiting bone formation in the BF EXO group, such as Ocu-miR-

133a-3p, Ocu-miR-133a-3p, Ocu-miR-143-3p, Ocu-miR-199a-3p, Ocu-miR-27b-3p, and Ocu-miR-21-5p. Furthermore, the improved osteoinductive capacity of BF EXO may be involved in the RTK/Ras/MAPK pathway, BMP/Smad pathway, WNT/β-catenin pathway, etc (Fig. 4D; **Table S5, Supporting Information**) [17–19]. Additionally, it was found that the 7 most up-regulated miRNAs promoting angiogenesis were Ocu-miR-486-5p, Ocu-miR-93-5p, Ocu-miR-25-3p, Ocu-miR-103a-3p, Ocu-miR-142-5p, Ocu-miR-92a-3p, and Ocu-miR-142-3p, in order of precedence. In turn, the 5 most downregulated miRNAs inhibiting angiogenesis were Ocu-miR-143-3p, Ocu-miR-199a-3p, Ocu-miR-29a-3p, Ocu-miR-125b-5p, and Ocu-miR-148a-3p in precedence (Fig. 4C). Furthermore, the mechanisms by which these miRNAs enhance angiogenesis may be associated with the PI3K/AKT/STAT3 pathway, CCND2 pathway, IFG/VEGF pathway, etc (Fig. 4D; **Table S6, Supporting Information**) [20–22].

2.7. Ability on Bone Formation of SrTi Sc + EXO Composites *in Vivo*

Based on the aforementioned results, the composite scaffold was fabricated using SrTi Sc and BF EXO loaded in poloxamer-based hydrogel and scanned by TEM, which is depicted in Fig. 5A. Immediately, SrTi Sc + EXO composites were implanted into the 1.5 cm radial CBDs of rabbits (Fig. 5B). Procollagen type I N-terminal propeptide (P1NP) and C-terminal telopeptide fragments of type I collagen (CTX-1) are the serum markers of bone formation and bone resorption, respectively. Hence, we performed ELISA for detection of P1NP and CTX-1 at 3-, 6-, 9-, and 12-weeks post-implantation. Generally, the P1NP levels in the serum of the SrTi Sc + EXO group were significantly higher than those of the SrTi Sc or EXO group at different timepoints (Fig. 5C). As expected, the CTX-1 levels in the serum of the SrTi Sc and SrTi Sc + EXO groups were suppressed compared with the EXO group at 3- and 6-weeks post-implantation. However, the inhibitory effects on CTX-1 were not obvious in the SrTi Sc + EXO group versus EXO group at 9 and 12 weeks (Fig. 5D).

Furthermore, gross morphological observation, micro-CT and undecalcified bone sectioning (stained with methylene blue & fuchsin acid) were employed to evaluate bone regeneration at 6 and 12 weeks after surgery *in vivo* (**Figure S19, Supporting Information**). At 6 weeks post-surgery, there was several poroma surrounding the cubitus due to radial trauma in the BLANK and EXO groups, whereas little bone formation existed in the CBD region. However, in the SrTi Sc and SrTi Sc + EXO groups, new bone formation induced by osteoconduction and osteoinduction can be detected within the inside and surrounding of the scaffolds (Fig. 6A and 7A; **Figure S20, Supporting Information**). Consistent with the respective micro-CT images, Fig. 6C showed that the SrTi Sc + EXO composite scaffold exhibited significantly increased bone mineral density (BMD), bone mineral content (BMC), bone volume/total volume (BV/TV), trabecular thickness (Tb.Th), and trabecular number (Tb.N) in CBDs of radius, as compared with that of the SrTi Sc or EXO groups at 6 weeks post-surgery.

At 12 weeks post-surgery, the poroma surrounding the cubitus further decreased and the regions of the CBDs were mostly filled by connective tissue in the BLANK and EXO groups, as compared with those at 6 weeks post-surgery, due to malunion of the radius. Meanwhile, the bone regeneration outside the region

of CBDs, rather than the interior of the scaffolds, was further increased in the SrTi Sc group. By contrast, new bone formation continuously increased in the CBDs of the SrTi Sc + EXO group (Fig. 6B and 7B; **Figure S21, Supporting Information**). As depicted in Fig. 6C, the results of the microCT demonstrated that, compared with the SrSc Ti group or EXO group, the SrTi Sc + EXO group displayed a significantly higher BMD, BMC, BV/TV, and Tb.N, but lower BS/BV and Tb.Sp.

Accordingly, to further evaluate dynamic bone formation within 2 weeks post-surgery, calcein and alizarin-3-methyliminodiacetic acid were intravenously injected at 3 and 1 weeks before euthanasia, respectively. The respective images of double fluorescent labeling demonstrated that the fluorescent bands were thick, and that the intervals between the 2 bands were broader at 6 weeks post-surgery, as compared with those at 12 weeks post-surgery, which indicated that bone formation at 6 weeks post-surgery was generally more vigorous, than those at 12 weeks post-surgery (Fig. 8A). Moreover, the results of dynamic histomorphometric analyses demonstrated that the mineral apposition ratio (MAR) and bone formation ratio/bone surface (BFR/BS) in the SrTi Sc + EXO group was significantly increased compared with those of the SrTi Sc group or EXO group at 6- and 12-weeks post-surgery (Fig. 8B). Hence, bone regeneration induced by osteoconduction and osteoinduction with the SrTi Sc + EXO composite was better than when only one of these was implanted.

2.8. Ability on Revascularization of SrTi Sc + EXO Composites in Vivo

Furthermore, to evaluate revascularization within the CBDs, gels of high density were infused into the vessels of CBDs, and the newly formed vessels of CBDs were scanned by microCT. Generally, at 6- and 12-weeks post-surgery, the SrTi Sc + EXO and SHAM groups exhibited the most vessels among the 5 groups. However, there were least vessels in the BLANK group. Additionally, the vessels within the SrTi Sc and EXO groups were intermediate in number (Fig. 9A). The data evaluated by microCT showed that the SrTi Sc + EXO significantly increased the vessel numbers, vessel volume, vessel diameters, and vessel volume/ total volume ratio at 6- and 12-weeks post-surgery, as compared with those of the SrTi Sc or EXO groups (Fig. 9B).

3. Discussion

Bone homeostasis is preserved by maintaining a balance between the activity of osteogenesis and osteoclastogenesis. Clinically, Sr ions can act as a bioactive factor in promoting bone formation and inhibiting bone resorption *via.* administrated strontium ranelate orally. However, it is insufficient to local CBDs repair and exists many side effects for oral administration [23]. Here, we fabricated the 3D-printed Ti Sc and Sr was subsequently implanted into the superficial layer of the scaffolds. *In vitro* release assay, Sr was quickly dissolved in PBS within 10 days (no more than 1 μg/day), which exactly met the requirements for phase of early bone regeneration [24]. Moreover, the sustained release of Sr ions was in favor of CBDs repair by enhancing osteoconduction, osteoinduction, and fibroblastic suppression, which was consistent with many studies [25, 26]. Of note, in the SrTi Sc and SrTi Sc + EXO groups, new bone

formation induced by osteoconduction and osteoinduction can be detected within the inside and surrounding of the scaffolds, which could be due to spatial support provided by the scaffold and fibroblast suppression by Sr being essential for avoiding connective tissue invading the region of bone formation during the repair of large bone defects. However, we also found that the inhibitory effects on CTX-1 were not obvious in the SrTi Sc + EXO group versus EXO group at 9 and 12 weeks, which may be due to depletion of sustainably released Sr from the SrTi Sc + EXO composite.

Exosomes have been applied as promising therapeutic strategies in numerous disease models owing to their excellent treatment effect and biocompatibility [27–29]. However, exosomes isolation is especially difficult because of the low productivity and high costs. Therefore, there were enormous challenges in clinical application for exosomes. Notably, a recent study demonstrated that the concentration of sEXO was 10^2-10^3 times higher than that of exosomes extracted from the cell culture medium through any exosome isolation method [30]. In our present study, we also confirmed that the concentration of serum exosome was as high as 10^9 particles/mL, much higher than the one derived from cells. Hence, higher yields of sEXO may be a promising source for medical applications. Besides, BF EXO was gradually and continuously released from a poloxamers-based hydrogel that finally lasted for 96 h, which had a pivotal effect on the early stages of osteogenesis and angiogenesis for CBD repair.

Recently, to achieve good osteoinductivity, some research reported that exosomes were obtained from osteogenic differentiation of MSCs that was induced by chemical compounds in *vitro*, prior to being utilized for treatment of bone defects in *vivo* [7, 31]. However, osteogenic exosomes induced by chemical compounds rather than the natural osteogenic microenvironment, may have limited clinical translation potential due to safety issues and other possible side effects. Inversely, BF EXO indeed exhibited a better biocompatibility and was in favor of clinical application. Besides, specifically functionalized body fluid has recently exhibited promising therapeutic potential for some intractable diseases. For instance, infusing young cerebrospinal fluid (CSF) directly into aged brains improved memory function on ageing brain of mice [8]. Moreover, another landmark research also showed that exposure to young blood through heterochronic parabiosis induced stem cell revitalization and systemic rejuvenation of aged mice tissues.[9] In our study, sEXO at the stage of fracture healing was also a kind of specifically functionalized body fluid owned excellent osteogenesis and angiogenesis. Furthermore, to meet requirements on quick and effective repair of local CBDs, BF EXO was isolated from specifically functionalized sEXO and exerted a profound effect on CBD healing, due to their excellent capacity to induce bone formation and revascularization.

More importantly, this study further broadens the source and biomedical potential of specifically functionalized exosomes. Firstly, a sEXO bank can be established through blood products with sophisticated management. Moreover, specifically functionalized sEXO can be classified according to medical indications. For instance, degenerative diseases of elderly people, such as Alzheimer's, Parkinson's, osteoporosis, etc. can attempted to be treated with sEXO of younger people. Similarly, extensive and deep burn wounds can be treated using sEXO from people with minor burn healing. Certainly, treatment of intractable bone trauma can be tried with BF EXO. Taken together, characterized by

relatively potent, natural, and coupled osteogenic/angiogenic induction capacity, BF EXO, as a key factor of cell-free therapeutic strategy in this study, offer much promising clinical applications in bone defect repair.

Besides, we use NGS to explore the potential mechanisms by which BF EXO promote both osteogenesis and vascularization. NGS analysis demonstrated that BF EXO accelerated osteogenesis and angiogenesis through multi-targeted interactions among the various miRNAs, which avoided off-target effects of a single target via boosting of one type of miRNAs shuttled by exosomes [32].

4. Conclusion

Based on our “cell-free scaffold engineering” strategy, a composite scaffold was fabricated using SrTi sc and BF EXO loaded with poloxamers-based hydrogels to repair the CBDs of radius. The composite scaffold enhanced osteogenesis and suppressed osteoclastogenesis at an early stage by combined Sr ion and BF EXO release, which in turn enhanced osteoconduction, osteoinduction, and fibroblastic suppression via the sustained release of Sr ions. Furthermore, the revascularization of CBDs was improved by BF EXO, which exerted both pro-osteogenic and pro-angiogenic effects on CBD repair. Moreover, those effects were regulated by multi-target interactions of the various miRNAs shuttled by BF EXO. This therapeutic strategy combining SrTi Sc and BF EXO is an effective, biocompatible, and clinically feasible strategy for large bone defect repair. Meanwhile, this study also broadens the mode of delivery and biomedical potential of specifically functionalized exosomes like BF EXO. A sEXO bank for clinical therapy may be established owing to the relative abundance and natural characteristics of sEXO, with specifically functionalized sEXO being further classified according to indications.

5. Experimental Section

SrTi Scaffold Fabrication

Firstly, the radius of rabbit was scanned by microCT. Next, the standard triangulation language (STL) file on critical bone defects (CBDs) of the radius was generated and input into the EBM S12 system (Arcam AB, Sweden). Medical-grade Ti_6Al_4V powder (particle size 15–45 μm) was melted layer by layer and further solidified by cooling. Finally, the Ti Sc were fabricated successfully after being ultrasonically cleansed successively in acetone, ethyl alcohol and deionized water.

And then, Sr was sputtered into a superficial layer of Ti Sc by ion implantation using an industrial PVD system (CemeCon AG, Germany). The implantation energy was 60 keV and the retained dose of Sr was 1×10^{17} ions/cm^2. After that, SrTi scaffold was fabricated successfully.

Characterization of Scaffolds

The microstructure of scaffolds was observed with a stereoscope, and the surface morphology was imaged by scanning electron microscopy (SEM) (S-3000N, Hitachi, Japan). The chemical composition of

the scaffold surface was analyzed by energy dispersive spectroscopy (EDS). The porosity was analyzed using a mercury porosimeter (PoreMasterGT 60, Quantachrome Instruments, USA). The specific surface area was calculated using the N_2-BET method and the 3D surface roughness was characterized by microCT. The mechanical strength (3-point flexural test and compression test) was analyzed by a mechanical testing system (Landmark, MTS Inc., USA).

Serum Exosomes (sEXO) Extraction: All animal experiments were approved by the Animal Care and Use Committee of Peking University Health Science Center (approval number: LA2019018; Beijing, P. R. China). 20 male New Zealand white rabbits (25 weeks, 3.5 ± 0.3 kg) were obtained from Vital River Inc. (Beijing, P. R. China) and randomly grouped as CTRL (control) group and BF (bone fracture) group.

In order to extract exosomes during the fracture healing period, we first constructed a rabbit femoral fracture model according to previously described methodology.[33] Briefly, The rabbits were anaesthetized using pentobarbital sodium (30 mg/kg) and the left femurs were fractured by rongeur forceps, and a 4 cm intramedullary nail (RabbitNail, RISystem, Switzerland) was introduced and locked in the fractured left femur. Venous blood samples were collected up to 20 mL from rabbits of CTRL or BF groups on the 5th day after femoral fracture, once every week, a total of 4 times.

The sEXO was extracted by methods of ultracentrifugation. Briefly, the serum was separated and centrifuged at 3,000 rpm for 10 min at 4°C to remove blood cells. After that, the cells and cell debris were removed by centrifugation at 2000 × *g* for 20 min followed by a second centrifugation at 10,000 × *g* for 30 min at 4°C. Next, the supernatant was ultracentrifuged (Beckman, USA) at 100,000 × *g* for 80 min. The pellet was then washed with PBS to eliminate contaminated proteins and centrifuged at 100,000 × *g* for another 80 min.

Characterization of sEXO

The morphology of sEXO was observed by transmission electron microscopy (TEM) (H-7600; Hitachi). The concentration and particle size of sEXO were measured by NanosightNS300 (Malvern, UK). The typical exosome surface markers on TSG101, CD81, and CD9 were detected by WB analysis (CST, USA).

Preparation of Poloxamers-based Hydrogel

The poloxamers-based hydrogels were prepared as previously described [34]. Briefly, poloxamer 407 and 188 (BASF, Ludwigshafen, Germany), sodium chloride (Xiya Reagent Co., Ltd, Linyi, P. R. China) were added to distilled water with stirring at 4℃; and the final concentrations are shown in Table S4. After incubation overnight at 4°C, the gels were completely dissolved to form clear, viscous solutions. The sEXO was then added into poloxamers-based hydrogels at a concentration of 1.4×10^{11} particles / mL (amount of sEXO from about 100 mL serum of rabbits/ mL hydrogels).

Sr Ion and sEXO Release Testing

SrTi Sc were immersed in 10 mL of standard simulated body fluid (SBF) buffer and then incubated at 37°C under gentle shaking. For the analyses of Sr ions, small aliquots were removed during the 84-day experiment, and these were replaced with equivalent volumes of fresh solution. The concentration of Sr ions released from SrTi Sc was determined by an inductively coupled plasma emission spectrometer (ICP; Optima™ 8300, PerkinElmer, USA).

Additionally, the sEXO cumulative release was detected by the aforementioned methods. The concentration of sEXO was determined by NanosightNS300.

Cell Culture, Cell Proliferation, and Cell Uptake Assays

L929 cells were selected to assess cytotoxicity of scaffolds. Bone marrow-derived mesenchymal stem cells (BMSCs) were selected for detecting osteogenesis and RAW264.7 cells were selected for detecting osteoclastgenesis. Human umbilical vein endothelial cells (HUVECs) were used for examining angiogenesis. BMSCs and RAW264.7 cells were cultured in α-MEM (Gibco BRL/Invitrogen, Carlsbad, USA) supplemented with 10% (v/v) fetal bovine serum (FBS; Biowest, France). HUVECs and L929 cells were cultured in DMEM supplemented with 10% (v/v) FBS (Gibco-BRL) and antibiotics (100 U/mL of penicillin and 100 mg/mL of streptomycin, Sigma). All cells were cultured at 37℃ within a humidified atmosphere containing 5% CO_2.

The Cell Counting Kit-8 (Dojindo Laboratories, Kumamoto, Japan) was used according to the manufacturer's instructions and the light absorbance (optical density, OD) at 450 nm of the formazan dye product was used to compute the cell proliferation rate.

The exosomes were stained with DIL (red, Beyotime Bio, P. R. China) and BMSCs were stained with FITC (green) and DAPI (blue) (Abcam, UK). After that, the CTRL EXO or BF EXO was co-cultured with BMSCs for 6 h. The samples were then observed with a confocal fluorescence microscope (FV1000, Olympus, Tokyo, Japan).

Immunofluorescence Staining: Cells or nude mouse skins were fixed with 4% (w/v) paraformaldehyde for 10 min. Then, the samples were permeabilized with 0.2% (w/v) Triton X-100 for 20 min and then washed with PBS at 37°C for 30 min. For nude mouse skins, primary antibodies against CD31 (1:1000; Abcam) were incubated at 4°C overnight. For RAW264.7 cells, goat anti-rabbit FITC (1:1000; CST) were placed and incubated at 37°C for 30 min. After washing in PBS, the cellular nuclei of each sample were counterstained with DAPI. After staining, the samples were observed using a confocal fluorescence microscope (FV1000, Olympus, Tokyo, Japan).

Alkaline Phosphatase (ALP) Detection and Alizarin Red S (ARS) Staining

For osteoinduction assays, 10 mM β-glycerophosphate, 10 nM dexamethasone, and 50 μg/mL L-ascorbic acid were added to α-MEM supplemented with 10% (v/v) FBS, 100 U/mL penicillin, and 100 mg/mL streptomycin (GIBCO). BMSCs were seeded at 40,000 cells/well in 6-well plates. Next, the CTRL EXO or BF

EXO were added into the culture medium at a concentration of 7×10^9 particles/ mL (amount of sEXO from about 5 mL serum of rabbits/ mL). To assess ALP activity, the cells were then stained with anitrobluetetrazolium (NBT)/5-bromo-4-chloro-3-indolylphosphate (BCIP) staining kit (CoWin Biotech, P. R. China) after osteoinduction for 7 days. Additionally, the cells were stained with 2% Alizarin red S staining solution (Sigma-Aldrich, St. Louis, MO, USA) for AOIR-S staining, after osteoinduction for 14 days.

Tartrate-resistant Acid Phosphatase (TRAP) Staining

RAW264.7 were seeded in 48-well plates at a density of 1×10^4 cells/well. RANKL (50 ng/mL) were added after 24 h for osteoclast induction of RAW264.7 for 4 days.

Osteoclastic differentiation of RAW264.7 was evaluated by TRAP staining using the Leukocyte Acid Phosphatase Kit (Sigma-Aldrich, St. Louis, MO, USA) and TRAP activity assay (TRAP Assay Kit; Takara, Shiga, Japan). Cultured cells were fixed in 3.7% paraformaldehyde for 10 minutes, treated with 0.1%Triton X-100 for 5 minutes, and rinsed 3 times with deionized water. Finally, cells were incubated with 0.01% naphthol AS-MX phosphate and 0.05% fast red violet LB salt in 50mM of sodium tartrate and 90mM of sodium acetate (pH 5.0) for 1 hour at 37 ℃ and rinsed 3 times with deionized water. TRAP activity was measured by using the cell culture supernatant generated after staining.

Real-time PCR: Total RNA was extracted by TRIzol reagent (Invitrogen, California, USA) and first-strand cDNA was then synthesized using a Prime Script RT Reagent Kit (Takara, Tokyo, Japan). After that, quantitative real-time polymerase chain reaction (RT-PCR) was performed using a 7500 Real-Time PCR Detection System (Applied Biosystems, Foster City, CA, USA). The following thermal settings were used: 95℃ for 10 min, followed by 40 cycles of 95℃ for 15 s and 60℃ for 1 min. Primer sequences used in RT-PCR are shown in Table S7. The data were analyzed using the $2^{-\Delta CT}$ method utilizing GAPDH as the housekeeping gene for normalization.

Scratch Test

The cells were seeded in 6-well plates and were cultured to cover the bottom of the plate. After 4–6 hours of starvation in serum-free medium, the HUVECs were scraped with a 100 μL sterile micropipette tip. Next, the cells were treated with CTRL EXO or BF EXO. Then, at 0, 3, and 6 hours, migratory cells were observed under an inverted microscope (OLYMPUS, Japan) and analyzed by using Image-Pro Plus 6.0 software (Maryland, USA).

Transwell Migration Assay

To investigate the effects of sEXO on the migration of HUVECs, transwell migration assay was performed. Briefly, $1x10^4$ cells cultured in serum-free medium were added to the upper chamber in a transwell system (BD falcon, USA) and migrated for 8 h. The cells on the upper chamber were removed and the remaining cells on the undersurface of the transwell were fixed using 4% (w/v) PFA. After staining using 0.2% (w/v) crystal violet, the migrated cells were visualized under bright-field microscopy.

Tube Formation Assay

Based on the manufacturer's instructions, frozen BD Matrigel™ (Growth Factor Reduced, #356231, USA) was melted into liquid at 4°C, and 10 μL of Matrigel was added to the bottom of each vasculogenic glass slide. After the matrigel solidified, the cell suspension (10^4 cells/well) was added, and the cells were treated with CTRL EXO or BF EXO for 24 hours. An inverted microscope was used to evaluate tube formation. Image-Pro Plus 6.0 software (Maryland, USA) was used to determine the number of tubes.

Matrigel Plug Assay

200 μL of Matrigel containing 30 IU/mL heparin (Sigma, USA), 1 μg/mL VEGF (Sigma) and CTRL EXO or BF EXO (about 2.8×10^{10} particles) was subcutaneously injected into 8-week old male nude mice. After 7 days, the Matrigel plugs were excised for immunofluorescence analyses. Additionally, photographs of newly formed vessels on the skins of nude mice were taken by a digital camera (Cannon, Japan).

Chicken Chorioallantoic Membrane (CAM) assay: Fertilized chicken eggs (Dafeng Breeding Co. Ltd, Beijing, P. R. China) were used to perform the CAM assay. A window with diameter of 1 cm was opened in the eggshell. Next, 100 μL of primary medium (PM) with CRTL EXO or BF EXO (about 1.4×10^{10} particles) was added into the CAM and then the window was closed using a piece of sterile adhesive tape. Eggs were placed in a 37 ℃ incubator with 80% humidity. After 4 days, CAMs were fixed by a mixed solution (methanol: acetone = 1:1) for 15 min before it was harvested. Photographs were taken with a digital camera (Cannon, Japan).

Next-Generation Sequencing (NGS) for sEXO

The NGS (Wayen Biotechnologies, Shanghai, P. R. China) was applied to explore the miRNA expression. First, the miRNA library were constructed through the QIAseq miRNA Library Kit. Next, the raw fastq data quality was handled by the Cutadapt, perl5, and bowtie software. The normalization and quantification of miRNA was carried out by comparison of the miRBse database. Meanwhile, the edgeR program was further used to identify differentially expressed genes. Genes with a fold change of expression more than 1.5 was defined as being differentially expressed.

Animals and Surgical Procedures: A total of 100 adult male New Zealand white rabbits (25 weeks, 3.5 ± 0.3 kg) were obtained from Vital River Inc. (Beijing, P. R. China) and were randomly assigned to 5 groups (20 rabbits for each group): 1) CTRL group (healthy rabbits); 2) BLANK group (rabbits of radial defects without any treatment); 3) SrTi Sc group (rabbits of radial defects treated with implantation of SrTi Scaffold); 4) EXO group (rabbits of radial defects treated with BF EXO loaded in poloxamers-based hydrogels); 5) SrTi Sc + EXO group (rabbits of radial defects treated with composite on SrTi Scaffold and BF EXO loaded in poloxamers-based hydrogels). Firstly, a rabbit large bone defect model was performed according to standard procedures. Briefly, the rabbits in each group were anesthetized by intravenous (i.v.) injection of pentobarbital sodium (30 mg/kg). Then, the rabbits' fur was excised from the front limb to expose the radius. The periosteum of the bone surface was peeled off, and a 1.5-cm bone defect within

the left radial midshaft was created. Meanwhile, the sterile SrTi Sc was immersed into poloxamers-based hydrogels containing BF EXO on ice. Immediately, the aforementioned composite or other materials were precisely implanted into the radius defect. Finally, the periosteum, muscle, and skin were sutured in sequence and antibiotics were injected to prevent infection.

At 6 weeks after surgery, 50 rabbits were randomly euthanized (10 rabbits of each group), the serum were collected, and the left radius were excised. Briefly, 5 rabbits in each group were subjected to micro-CT and subsequent processing of undecalcified histological slices. Other 5 rabbits in each group were operated for vascular infusion and then analyzed by micro-CT. The same procedures were carried out at 12 weeks as at 6 weeks.

Assay on Serum Biochemical Markers of Bone Turnover

To evaluate the serum biochemical markers of bone turnover, the associated ELISAs on procollagen type I N-terminal propeptide (P1NP) and C-terminal telopeptide fragments of type I collagen (CTX-1) (IDS, Frankfurt, Germany) were performed according to the manufacturer's instructions.

Micro Computed Tomography (CT) Analysis: To explore the differences in bone mass and microarchitecture among these groups, an Inveon MM system (Siemens, Munich, Germany) of the microCT was used to detect the specimens. Briefly, images of bone defects were scanned with a pixel size of 8.82 μm, current of 500 μA, voltage of 80 kV, and exposure time of 1500 ms in each of the 360 rotational steps. 1536 slices were contained in each projection and had a voxel size of 8.82 μm in all three axes. Three-dimensional (3D) visualization images were reconstructed in two-dimensional images and the parameters were calculated using Inveon Research Workplace (Siemens) as follows: bone mineral density (BMD), bone mineral content (BMC), bone volume/total volume (BV/TV), trabecular number (Tb.N), bone surface area/bone volume (BS/BV), trabecular separation (Tb.Sp), and trabecular thickness (Tb.Th) of newly-formed bone; vessels volume, vessels volume/total volume ratio, vessels numbers, and vessels diameters of newly-formed vessels within the region of radial defects.

Histology

First, the rabbits were injected with calcein (20 mg/kg BW, i.v.) and alizarin-3-methyliminodiacetic acid (30 mg/kg BW, i.v.) at 3 and 1 weeks before euthanasia, respectively. After euthanasia, the radius was fixed, dehydrated, and embedded in destabilized methyl methacrylate resin to make slices of undecalcified bones. Next, the slicings were grounded and polished to 50 μm using an EXAKT precision cutting and grinding system (EXAKT Apparatebau, Hamburg, Germany) and stained with methylene blue & fuchsin acid. Moreover, the mineral apposition rate (MAR) and bone formation rate/bone surface (BFR/BS) ratio were computed using the Bioquant software (BioQuant, San Diego, CA, USA).

Lead Tetroxide Infusion for Detection of Newly-formed Vessels

The rabbits received subcutaneous injections of 1000 IU/kg heparin (Sigma). Next, the proximal inferior vena cava and artery of rabbits were ligatured, and a 24-gauge indwelling needle was cannulated into the

left ventricle. Meanwhile, the right atrium was cut to make a tiny slit using ophthalmic scissors. Next, utilizing a peristaltic pump (Harvard Apparatus, South Natick, Massachusetts, USA), approximately 150 mL of pre-warmed normal saline, 100 mL of neutral formalin, and 50 mL of high-density lead tetroxide contrast solution were infused successively through the circulatory system. The contrast agent was 40% (w/v) Pb_3O_4 and 5% (w/v) gelatin in normal saline. After incubation overnight at 4°C, the radius from each rabbit was dissected and fixed in 10% (w/v) neutral-buffered formalin. The samples were subsequently scanned by micro-CT.

Statistical Analysis

All results are presented as the mean ± SD and were analyzed using SPSS 17.0 software (SPSS Inc., USA). Comparisons between two groups were performed using an unpaired Student's t-test. One-way ANOVA was used for comparisons among three or more groups. *$P < 0.05$ was regarded as statistically significant, and **$P < 0.01$ was regarded as highly significant.

Declarations

Ethics approval and consent to participate All animal experiments in this study were approved by the Animal Care and Use Committee of Peking University Health Science Center (Approval number: LA2019018, Beijing, China).

Consent for publication All authors agreed for publication.

Availability of data and materials Authors collectively declare that all data supporting the review article are available within the paper and its supplementary information files.

Competing interests All authors declare that they do not have any conflict of interest.

Funding This research was financially supported by the National Natural Science Foundation of China (Nos. 81930026, 82170929, 81970908), Peking University Medicine Fund for Fostering Young Scholars' Scientific & Technological Innovation (No. BMU2022PY010), and the Fundamental Research Funds for the Central Universities (No. PKU2022XGK008).

Authors' contribution Y.S.L and Y.S.Z designed the experiments, H.L. and R.L.G. performed the experiments, W.L, L.J.Z, Y.Z, B.C.H, analyzed the data. H.L., R.L.G., X.N.L. and S.Y.W wrote the manuscript. All authors have read and approved the final manuscript.

Acknowledgements Not applicable.

Supporting Information

Supporting Information is available from the Wiley Online Library or from the author.

References

1. Migliorini, F., et al., *Strategies for large bone defect reconstruction after trauma, infections or tumour excision: a comprehensive review of the literature.* Eur J Med Res, 2021. **26**(1): p. 118.
2. Norris, B.L., et al., *Treatments, cost and healthcare utilization of patients with segmental bone defects.* Injury, 2021. **52**(10): p. 2935-2940.
3. Chen, J., et al., *In Vitro Study on the Piezodynamic Therapy with a BaTiO3-Coating Titanium Scaffold under Low-Intensity Pulsed Ultrasound Stimulation.* ACS Appl Mater Interfaces, 2021. **13**(41): p. 49542-49555.
4. Chang, B., et al., *Influence of pore size of porous titanium fabricated by vacuum diffusion bonding of titanium meshes on cell penetration and bone ingrowth.* Acta Biomater, 2016. **33**: p. 311-21.
5. Lode, A., et al., *Strontium-modified premixed calcium phosphate cements for the therapy of osteoporotic bone defects.* Acta Biomater, 2018. **65**: p. 475-485.
6. Kalluri, R. and V.S. LeBleu, *The biology, function, and biomedical applications of exosomes.* Science, 2020. **367**(6478).
7. Zhai, M., et al., *Human Mesenchymal Stem Cell Derived Exosomes Enhance Cell-Free Bone Regeneration by Altering Their miRNAs Profiles.* Adv Sci (Weinh), 2020. **7**(19): p. 2001334.
8. Iram, T., et al., *Young CSF restores oligodendrogenesis and memory in aged mice via Fgf17.* Nature, 2022. **605**(7910): p. 509-515.
9. S. Ma, S.W., Y.X. Ye, J. Ren, R.Q. Chen, W. Li, J.M. Li, L.Y. Zhao, Q. Zhao, G.Q. Sun, Y. Jing, Y.S. Zuo, M.Z. Xiong, Y.H. Yang, Q.R. Wang, J.H. Lei, S.H. Sun, X. Long, M.S. Song, S.Y. Yu, P. Chan, J.W. Wang, Q. Zhou, J.C.L. Belmonte, J. Qu, W.Q. Zhang, G.H. Liu, *Heterochronic parabiosis induces stem cell revitalization and systemic rejuvenation across aged tissues.* Cell Stem Cell, 2022.
10. Geng, T., et al., *Exosome Derived from Coronary Serum of Patients with Myocardial Infarction Promotes Angiogenesis Through the miRNA-143/IGF-IR Pathway.* Int J Nanomedicine, 2020. **15**: p. 2647-2658.
11. Zhang, J. and X. Zhang, *Ischaemic preconditioning-induced serum exosomes protect against myocardial ischaemia/reperfusion injury in rats by activating the PI3K/AKT signalling pathway.* Cell Biochem Funct, 2021. **39**(2): p. 287-295.
12. Cheng, A., et al., *Impaired bone healing following treatment of established nonunion correlates with serum cytokine expression.* J Orthop Res, 2019. **37**(2): p. 299-307.
13. Working, Z.M., et al., *A quantitative serum biomarker of circulating collagen X effectively correlates with endochondral fracture healing.* J Orthop Res, 2021. **39**(1): p. 53-62.
14. Burska, A.N., et al., *Dynamics of Early Signalling Events during Fracture Healing and Potential Serum Biomarkers of Fracture Non-Union in Humans.* J Clin Med, 2020. **9**(2).
15. Stewart, C.C., et al., *Serum 25(OH)D is associated with an altered bone turnover marker response after a hip fracture.* J Orthop Res, 2019. **37**(3): p. 535-540.

16. Moghimi, S.M. and A.C. Hunter, *Poloxamers and poloxamines in nanoparticle engineering and experimental medicine.* Trends Biotechnol, 2000. **18**(10): p. 412-20.
17. Liao, W., et al., *BMSC-derived exosomes carrying microRNA-122-5p promote proliferation of osteoblasts in osteonecrosis of the femoral head.* Clin Sci (Lond), 2019. **133**(18): p. 1955-1975.
18. Chen, J., et al., *Exosomal miRNA-486-5p derived from rheumatoid arthritis fibroblast-like synoviocytes induces osteoblast differentiation through the Tob1/BMP/Smad pathway.* Biomater Sci, 2020. **8**(12): p. 3430-3442.
19. Liu, J., et al., *Downregulation of LINC00707 promotes osteogenic differentiation of human bone marrowderived mesenchymal stem cells by regulating DKK1 via targeting miR103a3p.* Int J Mol Med, 2020. **46**(3): p. 1029-1038.
20. Jin, Y.P., et al., *miR-143-3p targeting of ITGA6 suppresses tumour growth and angiogenesis by downregulating PLGF expression via the PI3K/AKT pathway in gallbladder carcinoma.* Cell Death Dis, 2018. **9**(2): p. 182.
21. Li, Q., et al., *Small extracellular vesicles containing miR-486-5p promote angiogenesis after myocardial infarction in mice and nonhuman primates.* Sci Transl Med, 2021. **13**(584).
22. Lacerda, J.Z., et al., *Therapeutic Potential of Melatonin in the Regulation of MiR-148a-3p and Angiogenic Factors in Breast Cancer.* Microrna, 2019. **8**(3): p. 237-247.
23. Pilmane, M., et al., *Strontium and strontium ranelate: Historical review of some of their functions.* Mater Sci Eng C Mater Biol Appl, 2017. **78**: p. 1222-1230.
24. Wang, X., et al., *Role of mesenchymal stem cells in bone regeneration and fracture repair: a review.* Int Orthop, 2013. **37**(12): p. 2491-8.
25. Hassani, A., et al., *Interaction of alginate with nano-hydroxyapatite-collagen using strontium provides suitable osteogenic platform.* J Nanobiotechnology, 2022. **20**(1): p. 310.
26. Del Buffa, S., et al., *Design and characterization of a composite material based on Sr(II)-loaded clay nanotubes included within a biopolymer matrix.* J Colloid Interface Sci, 2015. **448**: p. 501-7.
27. Han, C., et al., *Exosomes and Their Therapeutic Potentials of Stem Cells.* Stem Cells Int, 2016. **2016**: p. 7653489.
28. Phinney, D.G. and M.F. Pittenger, *Concise Review: MSC-Derived Exosomes for Cell-Free Therapy.* Stem Cells, 2017. **35**(4): p. 851-858.
29. Nooshabadi, V.T., et al., *The extracellular vesicles-derived from mesenchymal stromal cells: A new therapeutic option in regenerative medicine.* J Cell Biochem, 2018. **119**(10): p. 8048-8073.
30. Tang, Y.T., et al., *Comparison of isolation methods of exosomes and exosomal RNA from cell culture medium and serum.* Int J Mol Med, 2017. **40**(3): p. 834-844.
31. Teotia, A.K., et al., *Exosome-Functionalized Ceramic Bone Substitute Promotes Critical-Sized Bone Defect Repair in Rats.* ACS Appl Bio Mater, 2021. **4**(4): p. 3716-3726.
32. Lagana, A., et al., *miR-Synth: a computational resource for the design of multi-site multi-target synthetic miRNAs.* Nucleic Acids Res, 2014. **42**(9): p. 5416-25.

33. Brady, J., et al., *The effect of haemorrhagic shock and resuscitation on fracture healing in a rabbit model: an animal study.* Bone Joint J, 2018. **100-B**(9): p. 1234-1240.
34. Xuan, J.J., et al., *Rheological characterization and in vivo evaluation of thermosensitive poloxamer-based hydrogel for intramuscular injection of piroxicam.* Int J Pharm, 2010. **395**(1-2): p. 317-23.

Scheme 1

Scheme 1 is available in the Supplementary Files section.

Figures

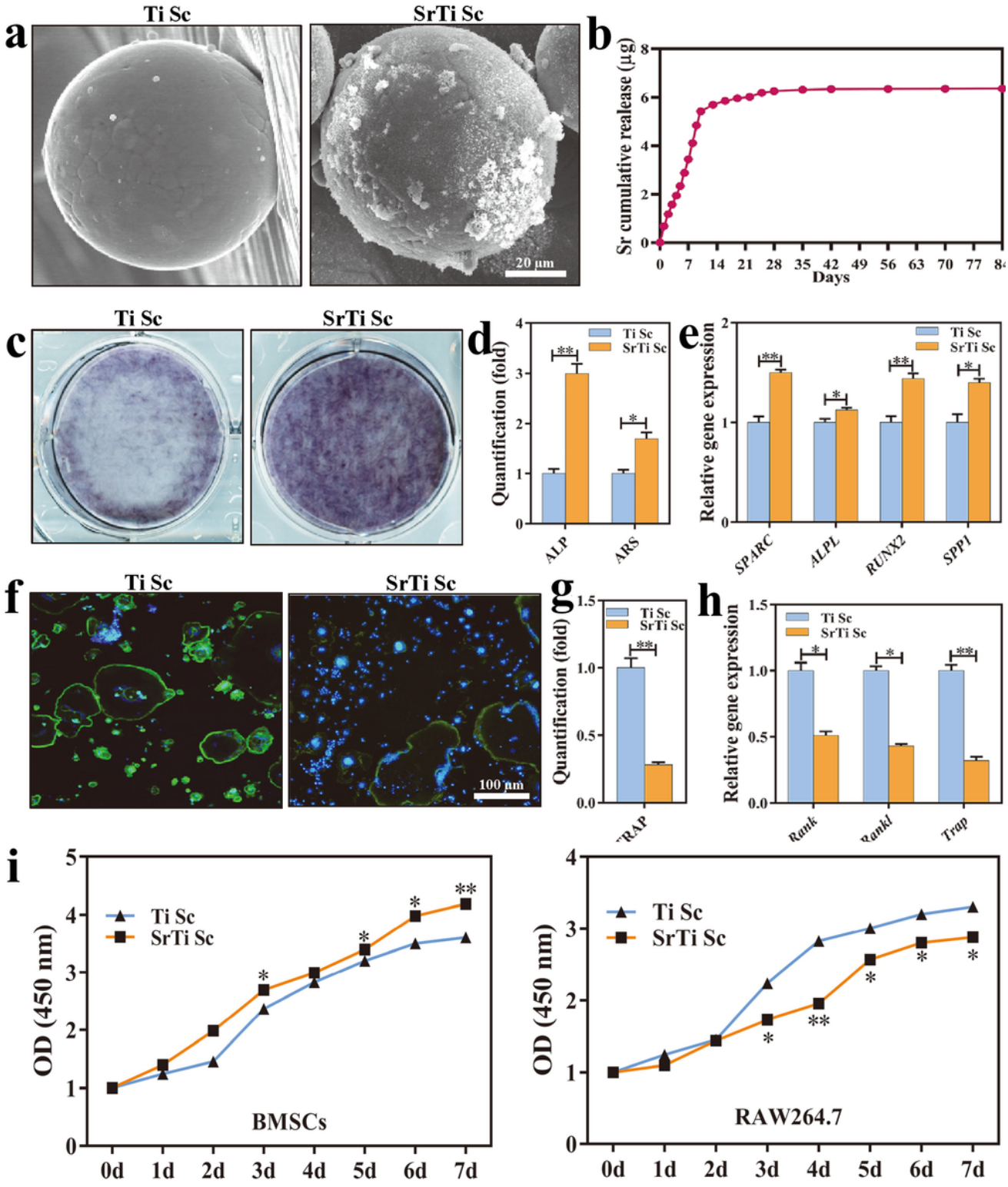

Figure 1

Sr ions released from **the** SrTi scaffolds promoted osteogenesis and suppressed osteoclast differentiation in *vitro*. (A) Representative SEM images of Ti Sc and SrTi Sc. Scale bar = 20 μm. (B) Cumulative release curve of Sr ions from SrTi Sc in *vitro*. (C) Representative images of ALP staining of BMSCs treated by leach liquorof Ti Sc or SrTi Sc. (D) Quantification of ALP and ARS staining of BMSCs treated by leach liquor of Ti Sc or SrTi Sc.(E) Relative osteogenic gene expression of co-cultured BMSCs

with leach liquorof Ti Sc or SrTi Sc. (F) Representative images of immunofluorescence staining for cell fusion of osteoclast co-cultured with RAW264.7, in the presence of leach liquorof Ti Sc or SrTi Sc. The osteoclast nuclei were stained by DAPI (blue), while the cytomembrane was stained by FITC (green). Scale bar = 100 μm. (G) Quantification of TRAP assay for RAW264.7 treated by leach liquor of Ti Sc or SrTi Sc. (H) Relative osteoclastic gene expression of RAW264.7 treated with leach liquorof Ti Sc or SrTi Sc. (I) The 7-day proliferation curve of BMSCs and RAW264.7 co-cultured with leach liquor of Ti Sc and SrTi Sc. All statistical data are presented as mean ± standard deviation (SD, n = 5 for (D), (E), (G), (H), and (I), $*P < 0.05$, $**P < 0.01$). ALP: alkaline phosphatase, ARS: alizarin red, BMSCs: bone marrow-derived mesenchymal stem cells, SEM: scanning electron microscopy, TRAP: tartrated resistant acid phosphatse.

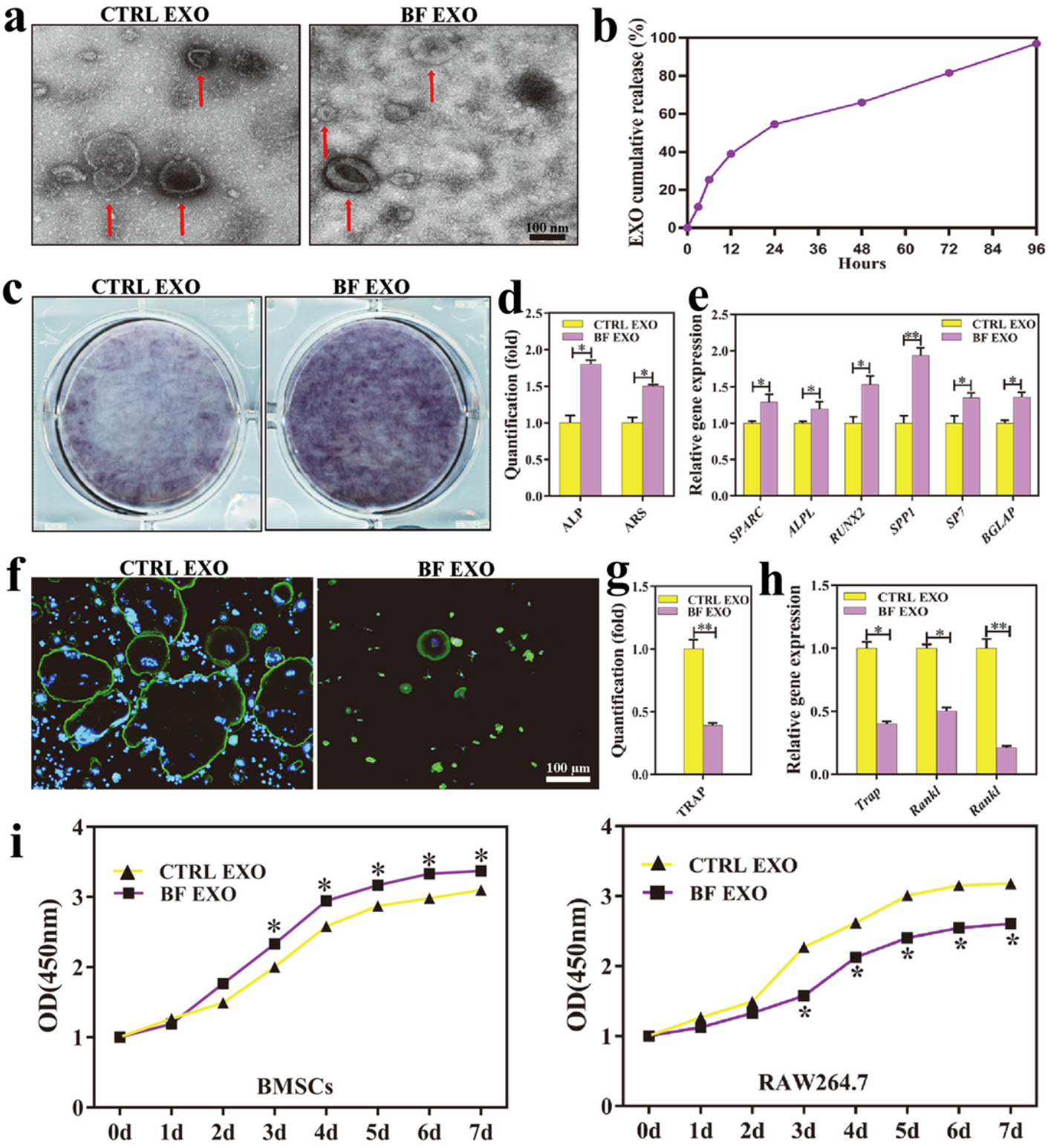

Figure 2

BF EXO enhanced osteogenesis and inhibited osteoclastogenesis in *vitro*. (A) Morphology of CTRL EXO and BF EXO visualized under TEM. The red arrows indicate exosomes. Scale bar = 100 nm. (B) EXO cumulative release curve from poloxamers-based hydrogel in *vitro*. C) Representative images of ALP staining of BMSCs treated with CTRL EXO or BF EXO. (D) Quantification of ALP and ARS staining for BMSCs treated with CTRL EXO or BF EXO. (E) Relative osteogenic gene expression of co-cultured BMSCs

with CTRL EXO or BF EXO. (F) Representative images of immunofluorescence staining for cell fusion of osteoclast co-cultured RAW264.7 with CTRL EXO or BF EXO. The osteoclast nuclei was stained by DAPI (blue) and the cytomembrane was stained by FITC (green). Scale bar = 100 μm. (G) Quantification of TRAP assay for RAW264.7 treated by CTRL EXO or BF EXO. (H) Relative osteoclast-related gene expression for RAW264.7 treated with CTRL EXO or BF EXO. (I) The 7-day proliferation curve of BMSCs and RAW264.7 co-cultured with CTRL EXO or BF EXO. All statistical data are presented as mean ± standard deviation (SD, n = 5 for (D), (E), (G), (H), and (I), $*P < 0.05$, $**P < 0.01$). ALP: alkaline phosphatase, ARS: alizarin red, BMSCs: bone marrow-derived mesenchymal stem cells, TEM: transmission electron microscope, TRAP: tartrated resistant acid phosphatse.

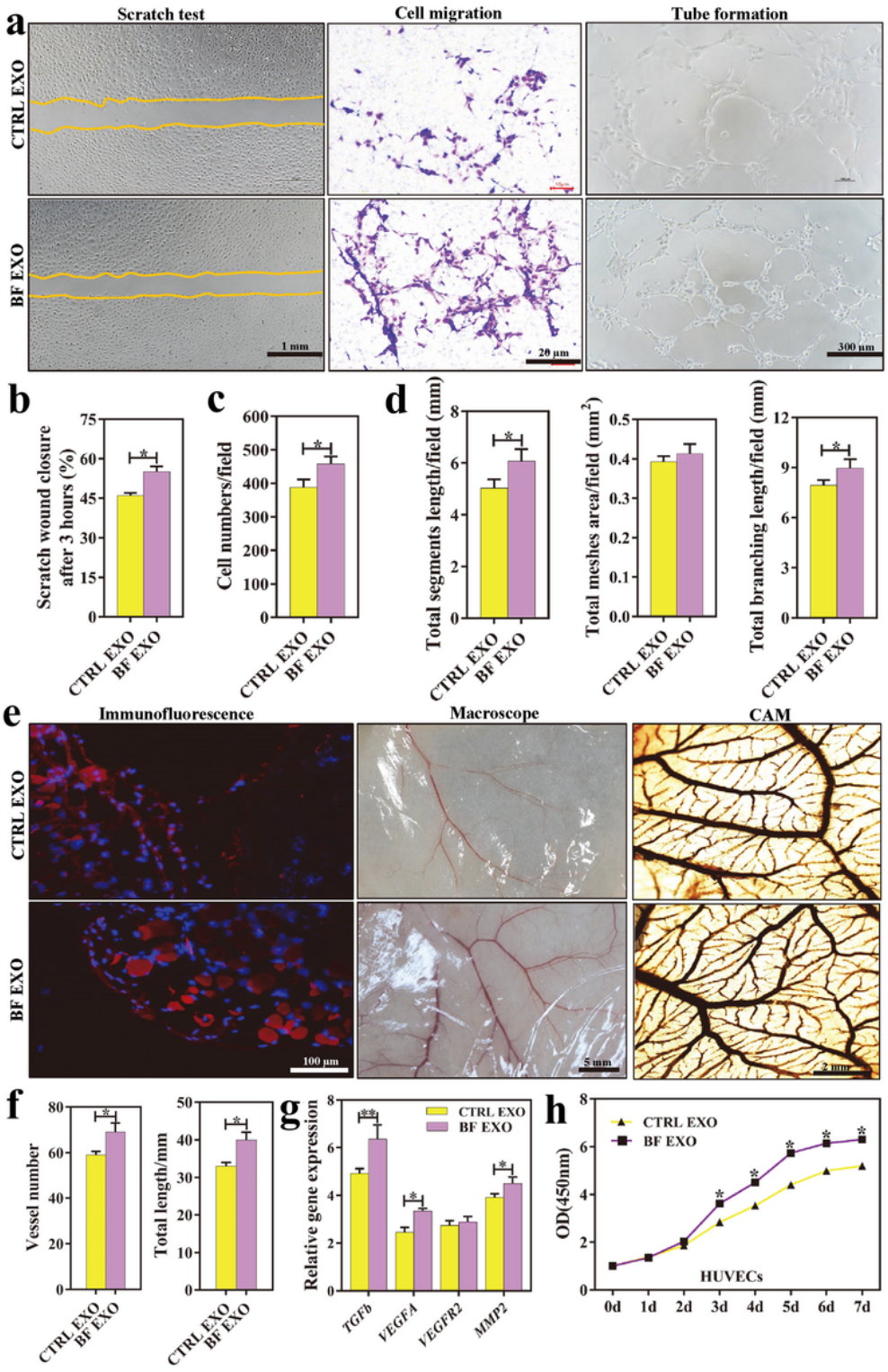

Figure 3

BF EXO significantly promoted angiogenesis both *vitro*and *vivo*. (A) Representative images of scratch test, transwell assay, and tube formation co-cultured HUVECs with CTRL EXO or BF EXO. Scale bar = 1 mm, 20 μm, and 300 μm, respectively. (B) Quantification of scratch wound closure for HUVECs treated by CTRL EXO or BF EXO in scratch test. (C) Counts of cells that migrated across the transwell membrane for HUVECs treated by CTRL EXO or BF EXO. (D) Tube formation quantification of total segment length, total

mesh area, and total branching lengths of HUVECs treated with CTRL EXO or BF EXO. (E) Representative images of immunofluorescence staining (left column) and photograph (middle column) of the skin of nude mice after subcutaneous injection of matrigel plug containing CTRL EXO or BF EXO for 7 days. The slicings were stained by anti-mouse CD31 antibody (red) and Hoechst 33342 (blue) to visualize VECs and cell nuclei, respectively. Scale bar = 100 μm and 5 mm. Additionally, representative images of neovascularization for CAM (right column) co-cultured with CTRL EXO or BF EXO. Scale bar = 2 mm. (F) Vessel number and total vessel length on CAM co-cultured with CTRL EXO or BF EXO. (G) Relative angiogenic gene expression for HUVECs treated with CTRL EXO or BF EXO. (H) The 7-day proliferation curve of HUVECs co-cultured with CTRL EXO or BF EXO. All statistical data are presented as mean ± standard deviation (SD, n = 5 for (B), (C), (D), (F), (G), and (H), *$P < 0.05$, **$P < 0.01$). CAM: chicken embryo chorioallantoic membrane, HUVECs: human umbilical vein endothelial cells, VECs: vein endothelial cells.

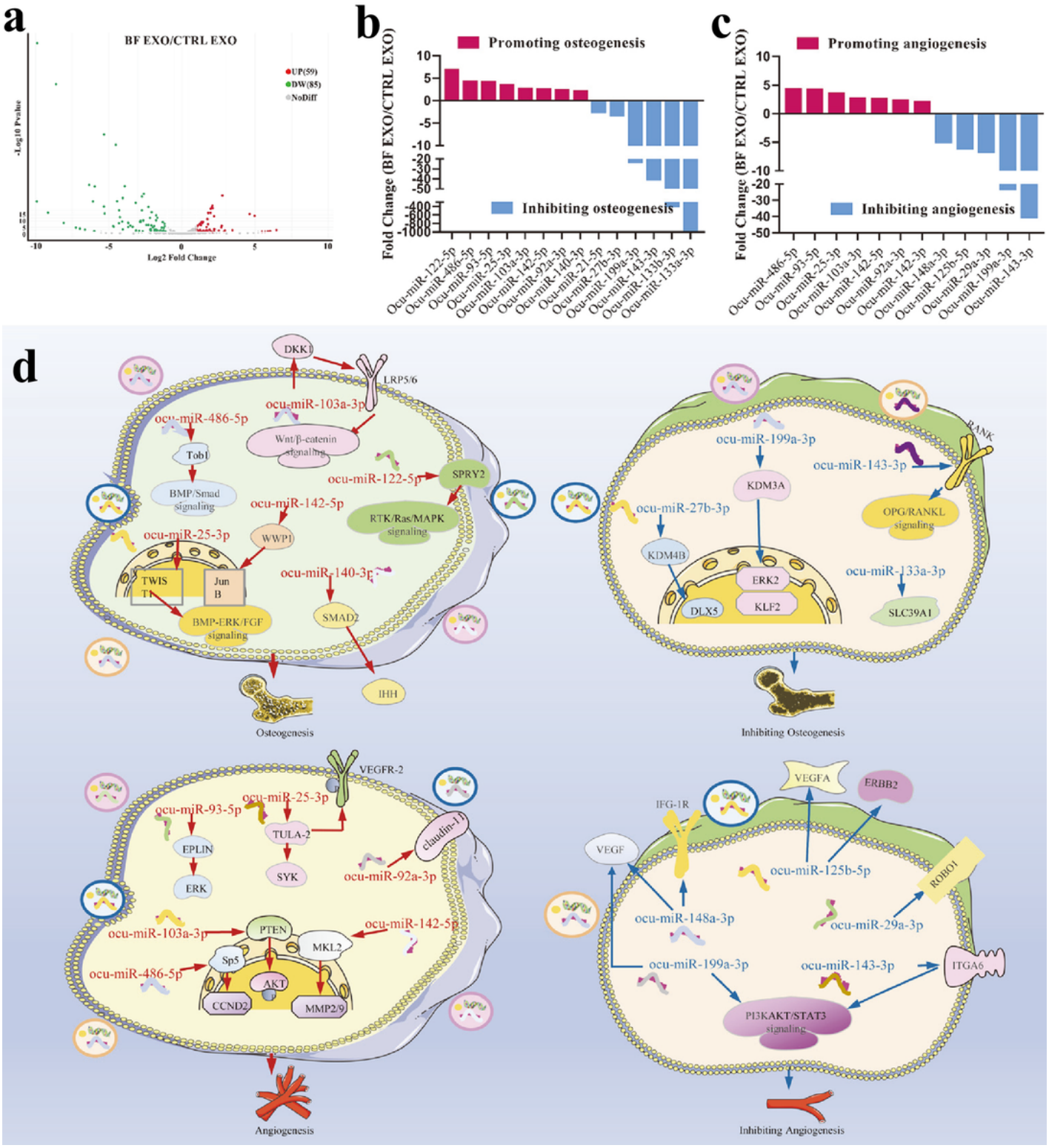

Figure 4

The potential pro-osteogenic and pro-angiogenic mechanisms of BF EXO, as detected by the NGS. A) Volcanic map of miRNA expression of BF EXO versus CTRL EXO. B) Concrete miRNAs that contributed to the most significant differences in osteogenesis between BF EXO versus CTRL EXO. C) Concrete miRNAs that contributed to the most significant differences in angiogenesis between BF EXO versus CTRL EXO.

D) Potential mechanism of miRNAs targeting on osteogenesis and angiogenesis. NGS: next generation sequencing.

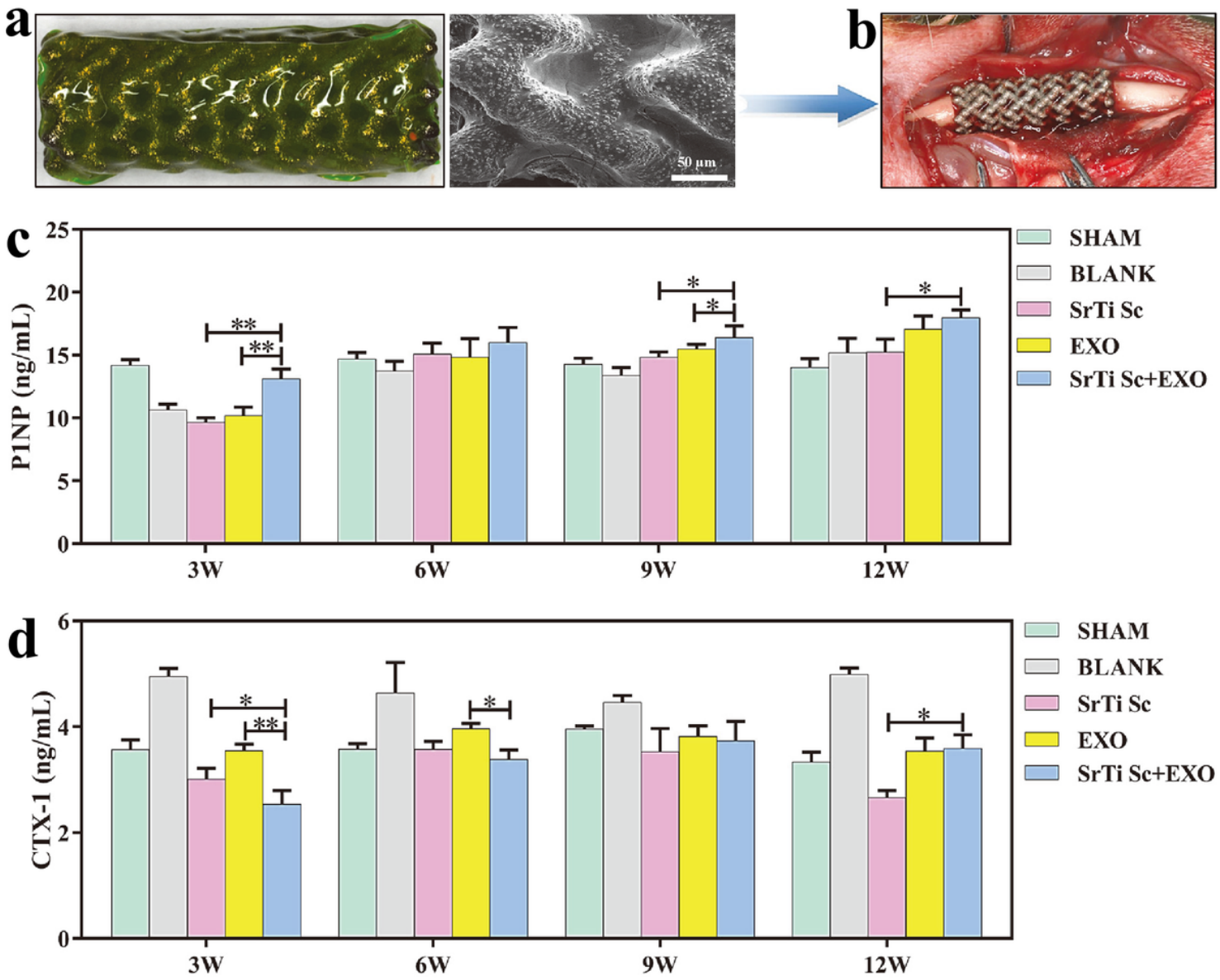

Figure 5

SrTi Sc+EXO composite scaffold up-regulated the levels of serum P1NP and down-regulated the levels of serum CTX-1 *in vivo.* A) Photograph and SEM images of the SrTi Sc+EXO composite scaffold. Green represents the poloxamer-based hydrogel containing BF EXO (the transparent hydrogel was stained with calcein to improve visualization). Scale bar = 50 μm. B) Intraoperative image of the SrTi Sc+EXO composite scaffold implanted into a critical radial defect of rabbit. C) Serum levels of osteogenic marker of P1NP in rabbits at 3, 6, 9, and 12 weeks post-surgery. D) Serum levels of osteoclastic marker of CTX-1 in rabbits at 3, 6, 9, and 12 weeks post-surgery. All statistical data are presented as mean ± standard deviation (SD, n = 5 for (C) and (D), **P* < 0.05, ***P*< 0.01 *vs.* SrTi Sc+EXO group). CTX-1: C-terminal

telopeptide fragments of type I collagen, P1NP: procollagen type I N-terminal propeptide, SEM: scanning electron microscopy.

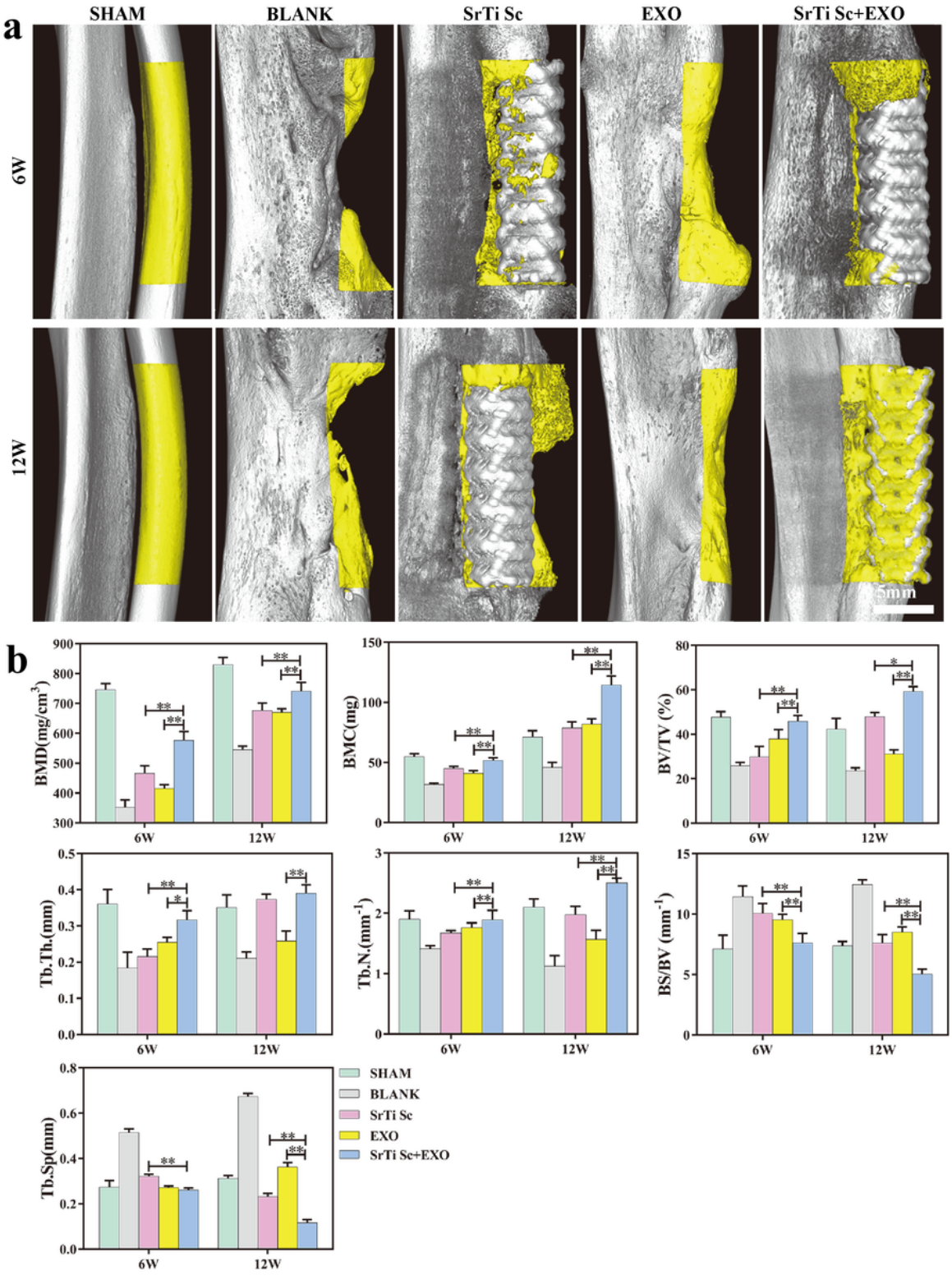

Figure 6

SrTi Sc+EXO composite scaffold promoted *in vivo* bone regeneration in CBDs of the radius at 6 and 12 weeks after surgery. Representative images of bone formation within CBDs of the radius of rabbits in

each group at 6 (A) and 12 (B) weeks after surgery, as detected by microCT (Yellow region represents bone on CBDs of radius of rabbits). Scale bar = 5 mm. C) Bone morphometry of new bone formation within the CBDs of radius. All statistical data are presented as mean ± standard deviation (SD, n = 5 for (B), *$P < 0.05$, **$P < 0.01$ *vs.* SrTi Sc+EXO group). CBDs: critical bone defects.

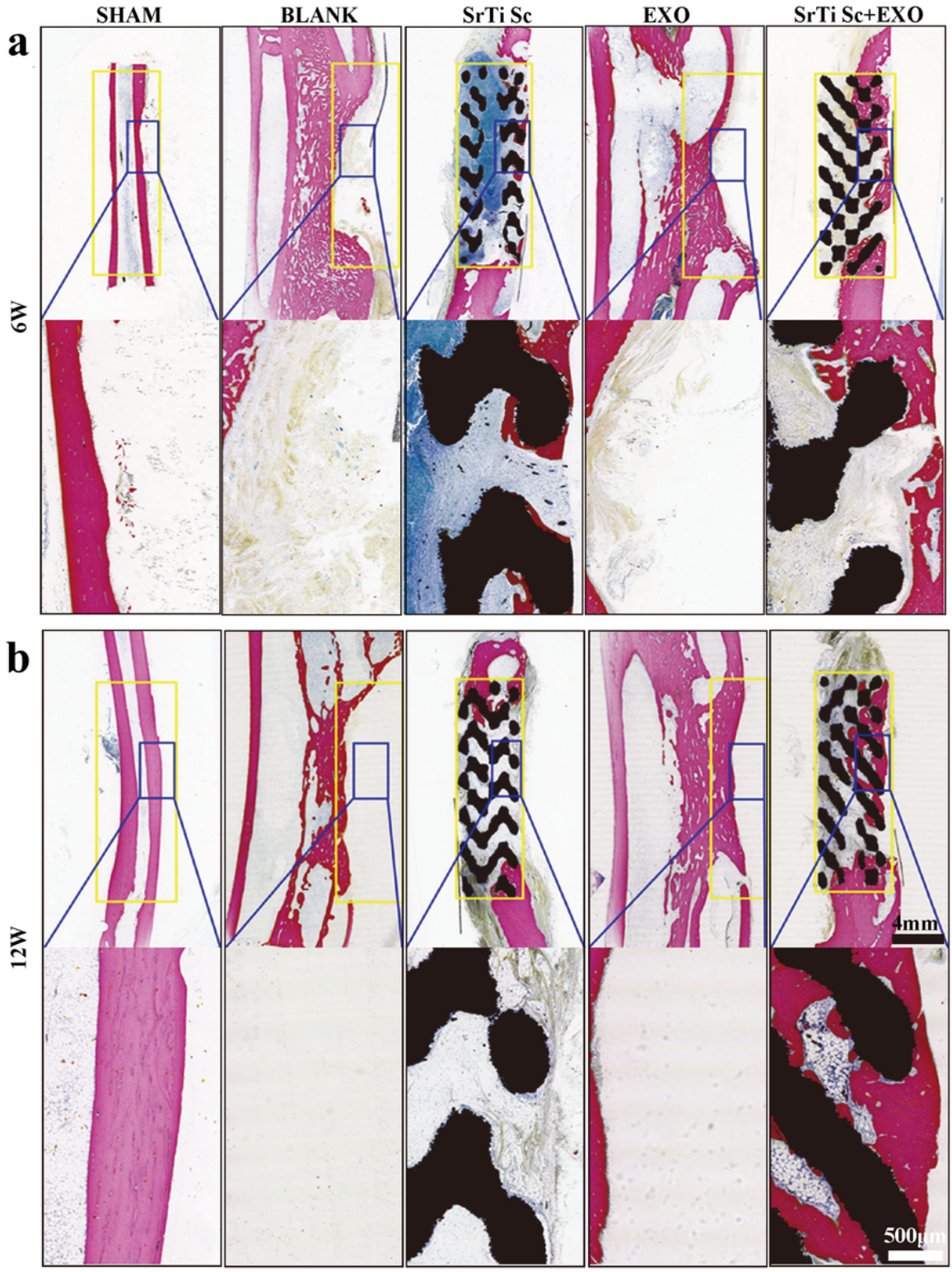

Figure 7

SrTi Sc+EXO composite scaffold promoted *in vivo* bone regeneration in the CBDs of radius for 6 (A) and 12 (B) weeks after surgery. Representative images of undecalcified bone slicings of new bone formation within the CBDs of the radius of rabbits in each group (stained by methylene blue & fuchsin acid, yellow box represents new bone formation within the CBDs of the radius of rabbits). Scale bar = 4 mm and 500 μm. CBDs: critical bone defects.

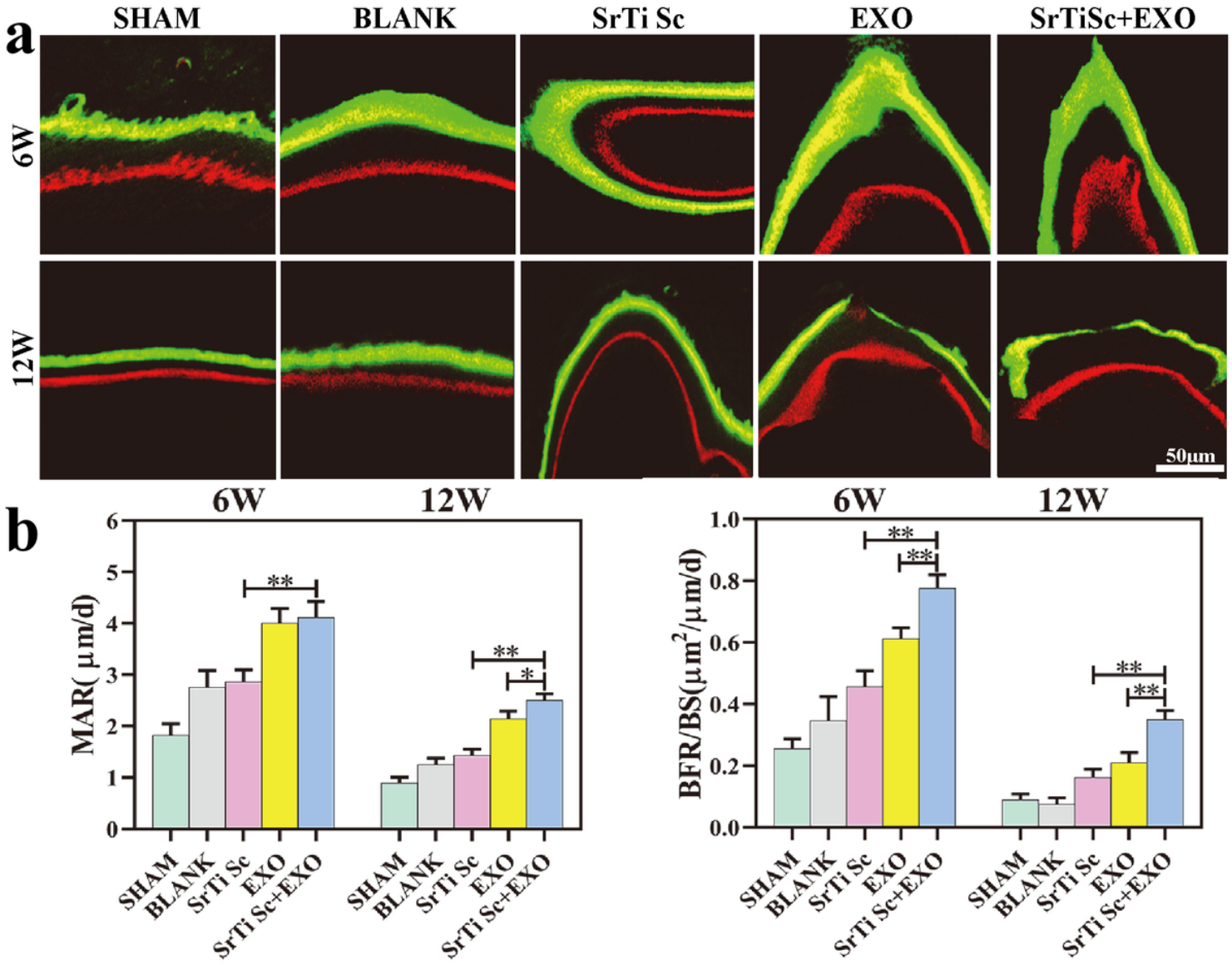

Figure 8

SrTi Sc+EXO composite scaffold improved the parameters of *in vivo* dynamic bone formation in the CBDs of radius. A) Representative images of double fluorescent labeling within the radial CBDs of rabbits in each group at 6 and 12 weeks post-surgery. Scale bar = 50 μm. B) Quantitative analysis of MAR and BFR/BS by double fluorescent labeling within the radial CBDs of rabbits in each group at 6 and 12 weeks post-surgery. All statistical data are presented as mean ± standard deviation (SD, n = 5 for (B), **P* < 0.05, ***P* < 0.01 *vs.* SrTi Sc+EXO group). BFR/BS: bone formation ratio/bone surface, CBDs: critical bone defects. MAR: mineral apposition ratio.

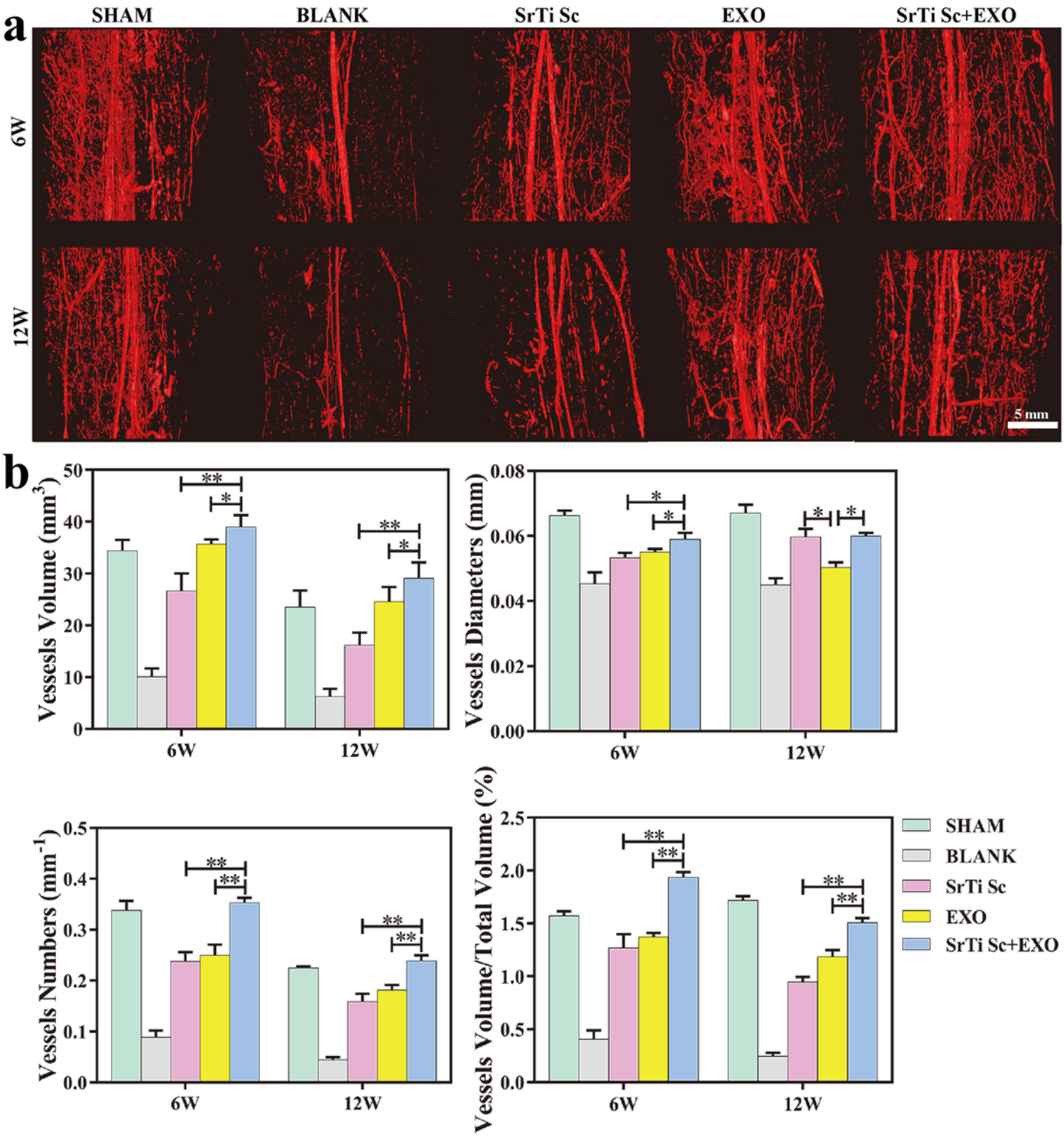

Figure 9

The SrTi Sc+EXO composite scaffold promoted *in vivo* neovascularization within the CBDs of radius. A) Representative images of the newly formed vessels within CBDs infused by gels of high density in each group at 6 and 12 weeks post-surgery, as detected by microCT. Scale bar = 5 mm. B) Analysis of vessel volume, vessel volume/ total volume ratio, vessel numbers, and vessel diameters at 6 and 12 weeks post-

surgery. All statistical data are presented as mean ± standard deviation (SD, n = 5 for (B), *P< 0.05, **P < 0.01 *vs.*SrTi Sc+EXO group). CBDs: critical bone defects.

Supplementary Files

This is a list of supplementary files associated with this preprint. Click to download.

- 1Scheme.tif
- SupportingInformationendonote.docx